AIAA A01-34608

AIAA 2001-4503

DEVELOPMENT AND TESTING OF PARAFFIN-BASED HYBRID ROCKET FUELS

M. A. Karabeyoglu, B. J. Cantwell, D. Altman
Department of Aeronautics and Astronautics
Stanford University
Stanford, California 94305

37th AIAA/ASME/SAE/ASEE
Joint Propulsion Conference and Exhibit
July 8-11, 2001/Salt Lake City, Utah

DEVELOPMENT AND TESTING OF PARAFFIN-BASED HYBRID ROCKET FUELS

M. A. Karabeyoglu[*], B. J. Cantwell[†], D. Altman[‡]
Department of Aeronautics and Astronautics
Stanford University
Stanford, California 94305

Abstract

The classical hybrid combustion theory is generalized to solid fuels that form a liquid layer on their burning surface. For several classes of liquefying fuels, the layer is hydrodynamically unstable leading to substantial droplet entrainment from the melt layer into the gas stream. The susceptibility of a given fuel to this shear driven instability increases with decreasing viscosity and surface tension of the melt layer. The entrainment mass transfer, which acts in addition to the conventional gasification mechanism, is not affected by the blocking phenomenon induced by blowing from the surface. For practical oxidizer flux levels encountered in hybrid rocket applications, droplet entrainment can dominate direct gasification. Such liquefying fuels can exhibit greatly increased surface regression rates compared to classical materials such as HTPB. One application of the theory is to solid cryogenic hybrids, which utilize frozen materials for the solid propellant. The theory successfully predicts why high regression rates are observed in tests of cryogenic solid pentane, solid pentane and solid oxygen. In addition, the theory explains the dependence of the burning rates of other tested cryogenic materials on the physical properties of the liquid layer. The theory also leads to the conclusion that certain non-cryogenic materials such as paraffin and PE waxes will also exhibit high regression rates. This important result is confirmed by lab scale tests performed at Stanford University on a paraffin-based fuel.

1) Nomenclature

a: Absorption coefficient, m^{-1}

a_{ent}:   Entrainment coefficient

B, B_g: Blowing parameter and evaporation blowing parameter

b: Regression rate parameter

C: Specific heat, kJ/kg-sec

C_{B1}, C_{B2}:   Blowing correction coefficients

C_H, C_{Ho}:   Stanton number with and without blowing

c: Amplification parameter

c_f: Skin friction coefficient

F_r: Heat transfer correction factor for surface roughness

d_p: Port diameter

Fr: Froude number

$f_g(\zeta)$:   Viscous solution for the gas phase Orr-Sommerfeld equation

$G, \overline{G}$:   Instantaneous mass flux, time averaged mass flux, kg/m²-sec

g: Body force per unit mass

h: Melt layer thickness, mm

h_v: Effective heat of gasification, kJ/kg

h_m, h_e: Effective heats, kJ/kg

Δh: Enthalpy difference between the flame and the surface, kJ

i: Unitary complex number

I: Gas phase velocity profile integral

k: Wave number, cm^{-1}

L_m, L_v: Latent heat of melting and vaporization, kJ/kg

$\dot{m}_{ent}$:   Entrainment component of mass flux from fuel surface, kg/m²-sec

$\dot{m}_l$:   Mass flow rate of liquid flowing through melt layer per unit width, kg/m-sec

O/F: Oxidizer to fuel ratio

P_d: Dynamic pressure in the port, Pa

$\overline{\tilde{P}}_g$:   Nondimensional gas phase normal stress perturbation

$\dot{Q}_r, \dot{Q}_c$:   Radiative and convective heat flux at the surface, kJ/m²-sec

---

[*] Post-doctoral fellow, Member AIAA
[†] Professor, Member AIAA
[‡] Consulting Professor, Fellow AIAA, President, Space Propulsion Group Inc.

$\dot{Q}_w$: Total heat flux at the surface, kJ/m²-sec
R: Ratio of thermal to radiative thickness
Re: Liquid layer Reynolds number
Re_g: Gas phase Reynolds number
R_{hv}, R_{he}: Ratio of effective heat of gasifications for entrainment and vaporization
$\dot{r}, \bar{\dot{r}}$: Instantaneous and time-averaged regression rate, mm/sec
$\dot{r}_{cl}$: Regression rate predicted by classical theory, mm/sec
T_a: Initial fuel temperature, K
T_g: Average gas phase temperature, K
T_m, T_v: Melting and vaporization temperatures, K
$U_o(y)$: Mean axial velocity of the liquid, m/sec
U_l, U_l^o: Mean axial velocity of the liquid at the interface with and without blowing, m/sec
$U_g(\zeta)$: Mean velocity of the gas flow, m/sec
U_g^o: Gas velocity at the center of the port, m/sec
V_l: Mean normal velocity of the liquid, m/sec
We: Weber number
X_e: Entrainment parameter, N$^{1/2}$
y: Distance from the interface, m
z: Axial distance along the port, m
α: Nondimensional wave number
$\hat{\alpha}, \hat{\beta}$: Dynamic pressure and thickness exponents
Δ: Gas phase stress perturbation parameter
δ_m: Liquid layer momentum thickness
$\phi(y)$: y-component of nondimensional liquid stream function
$\hat{\gamma}$: Viscosity exponent
η: Surface waveform
κ: Thermal diffusivity, m²/sec
μ: Viscosity, milliPa-sec
$\hat{\pi}$: Surface tension exponent
ρ: Density, kg/m³
σ: Surface tension, milliN/m
τ_g: Mean shear stress exerted by the gas flow on the liquid-gas interface
$\bar{\tau}_g$: Nondimensional gas phase shear stress perturbation
ψ: Nondimensional thickness parameter
$\psi_g(\zeta)$: Inviscid solution for the gas phase Orr-Sommerfeld equation
ζ: Normal curvilinear coordinate in the gas phase

Subscripts:
ent: Entrainment
g: Gas
l: Liquid
o: Oxidizer

s: Solid
v: Vaporization
Superscripts:
-: Nondimensional quantity

2) Introduction

Despite their safety and cost advantages over solid and liquid systems, conventional hybrid rockets possess one very significant shortcoming, very low fuel regression rates. For many practical applications, this leads to a complex, multi-port grain design such as the commonly used wagon wheel configuration. The multi-port design presents serious shortcomings, which significantly degrade the overall performance, reliability and cost effectiveness of a hybrid propulsion system. Some of the disadvantages of a multi-port configuration can be listed as:

- Large sliver fractions, which may in practice leave large quantities of fuel unburned.
- Fairly low volumetric loading of the fuel in the casing leading to low thrust densities.
- Fuel grain integrity problems, especially towards the end of the burn when the web thickness between ports becomes vulnerable to structural disintegration. A costly solution for this problem is to use web supports. This method, however, will compromise the system performance and will add weight and complexity.
- Difficult and expensive manufacturing of the fuel grain
- Requirement for a pre-combustion chamber or multiple injectors.
- Potentially non-uniform burning from port to port.
- Increased risk of instabilities related to multi-port dynamic interactions or due to the existence of a large pre-combustion chamber.

Fundamentally, the limit on regression rate for conventional hybrid fuels is set by the physical phenomena of heat and mass transfer from the relatively remote flame zone to the fuel surface[1]. Heat transfer to the fuel surface is further reduced by the well-known "Blocking Effect" which is induced by the radial blowing of a large quantity of gas from the fuel surface. As a consequence, the regression rates of modern hybrids that utilize polymers as the fuel are much lower than conventional solid rocket burning rates.

So far many techniques have been suggested or tried to increase the regression rates of hybrids. Unfortunately, all of these methods suffer important shortcomings. Some of these techniques are listed here.

2

- Use of fuel with low effective heat of gasification. This method yields only a modest improvement since, as revealed in the classical hybrid theory[1,24], the exponent of the heat of gasification is a small number (approximately 0.32). The weak dependency of the regression rate on the heat of gasification is due to the "Blocking Effect" described earlier.

- Insertion of screens or other mechanical devices in the port to increase the turbulence level and thus the heat transfer rates. This method complicates the design significantly and increases the likelihood of failure. In addition, this approach may lead to nonuniform burning along the port.

- Add swirl to the incoming oxidizer flow to increase the effective mass flux and thus improve the heat transfer rate. This method also complicates the hybrid design, especially for large scale motors, and requires heavy injectors or vanes.

- Addition of oxidizing agents or self decomposing materials in the hybrid fuel. This well known technique reverts to a quasi-solid design and eliminating the inherent safety characteristic of hybrid rockets. In addition, the regression rate becomes sensitive to chamber pressure.

- Addition of metal additives. This is also a common technique that improves the fuel mass burning rate. The improvement is small and there are several shortcomings such as the increased vulnerability to instabilities due to the pressure dependent regression rate and increased environmental impact. This is a separate consideration from the addition of metal additives to increase fuel density, which is a useful improvement.

- Increasing the roughness of the burning surface by adding dispersed solid particles in the fuel that would burn at a different rate compared to the matrix material. This technique can only give a limited improvement and large solid particles injected in the gas stream might reduce the efficiency of the system. Fuel grain manufacturing costs would also increase.

We believe that a natural and effective methodology to increase the regression rate is to carefully formulate a hybrid fuel that will generate mass transfer by mechanical means in addition to the mass transfer by direct gasification from the fuel surface. For materials forming a low viscosity melt layer on their burning surfaces, the mechanical mass transfer will take place by the entrainment of liquid droplets into the gas stream. An obvious class of entraining substances includes liquids or gases at standard conditions, which are frozen to form solids (i.e. solid cryogenic hybrids). Typical members of this class range from H_2, a deep cryogen, to liquid amines and hydrocarbons. However

it is clear that the same internal ballistic behavior can be experienced by materials that are solids at standard conditions if they form a low viscosity melt layer at the combustion surface.

In fact, increased regression rates by several hundred percent have been observed with solid cryogenic hybrids by researchers at the Air Force Research Laboratory (AFRL)[2,3,4] and ORBITEC[5,6]. The AFRL program was concentrated on burning several frozen organic liquids including normal pentane with gaseous oxygen in a small test motor. Fig. 1 shows the burning rate behavior of pentane and several other hydrocarbons tested by AFRL in the space-time averaged regression rate, $\bar{r}$, time averaged oxidizer mass flux $\bar{G}_o$, plane. Note that for the presented set of data, the averaged oxidizer mass flux is defined based on the average port radius. The regression rate law for a typical conventional hybrid fuel, HTPB, is also included in Fig. 1 for comparison purposes. A typical regression rate expression for an HTPB-O_2 hybrid[7], $\dot{r} = 0.025 G_o^{0.65}$ mm/sec where G_o is in kg/m²-sec (grain length = 15 cm), is used in the calculations. As shown in Fig. 1, the measured regression rates for cryogenic pentane are 3-4 times larger than the reported regression rates for the conventional fuel, HTPB, under the same oxidizer mass flux condition.

Similarly, ORBITEC conducted tests using solidified kerosene and methane with gaseous oxygen and solidified oxygen with gaseous methane (i.e. a reverse hybrid configuration) with small AFRL scale motors. In the process of developing a production technique for frozen methane fuel grains, ORBITEC also performed a limited number of tests with a low molecular weight paraffin wax. The oxidizer mass fluxes corresponding to the measured regression rates for the paraffin tests were not reported. Similar to the AFRL results, solid kerosene and methane showed very high burning rates relative to the polymeric classical hybrids.

We may conclude from these various experiments that the regression rates for cryogenic propellants are many times higher than for conventional hybrids. This observation cannot be explained by a lower heat of vaporization, which is insufficient to account for the observed regression rate increase. Recall that in the classical regression rate expression[1,24], the heat of vaporization is incorporated in the blowing parameter, B, raised to a power 0.32. We have estimated a maximum B value of 13.5 for the pentane-O_2 system using the expressions given in Ref. 1, which would only cause a minor increase in the regression rate (30-50 %) over the conventional systems rather than the

observed increases of 300-400%. A different mechanism is clearly indicated.

The regression rate model developed for these liquefying propellants, in addition to the classical gasification, is based on a mass transfer mechanism involving the entrainment of liquid droplets from the melt layer. As will be demonstrated, droplet formation is due to liquid layer instabilities, which result from the high velocity gas flow in the port. The purpose of this paper is to explore the development of the liquid layer at the burning surface and to determine the conditions for the onset of droplet entrainment so that its occurrence can either be invoked or avoided. A schematic of the presumed model for entrainment is shown in Fig. 2.

3) Development of the Liquid Layer Hybrid Combustion Theory

In this section we will describe the development of a theory that can be used to explain the phenomena observed in cryogenic hybrids and that will extend the applicability of the hybrid combustion theory to fuels that may form a reasonably thick liquid layer during their combustion. Due to the complexity of the problem, we will perform the development in three stages. In the first stage, we will investigate the requirements for the formation of a melt layer on the fuel grain. In the second stage, we will consider the linear stability of a melt layer under the strong shear of a gas flow. The linear stability model discussed in the following paragraphs includes the effect of the injection of liquid at the liquid-solid interface due to the regression of the fuel slab. Later in this stage the linear stability results will be linked to the entrainment of liquid droplets with use of some experimental results and some semi-empirical relations developed in the nuclear engineering literature. Eventually in the final stage, classical theory will be extended to the case of liquid droplet entrainment. It is shown that the primary effect of the entrainment mass transfer is to increase the regression rate of the fuel without materially increasing the thermochemically defined blowing parameter, B. Note that the thermochemical blowing parameter can only be altered, to some degree, by changing the thermochemical properties of the propellants or the combustion parameters such as the local flame O/F ratio.

A) Liquid Layer Thickness Estimation

In this section the thermal analysis to estimate the film thickness formed on a burning slab under the combined heating by convection and radiation is summarized. The thickness of the liquid layer can be determined by the energy transfer relations in the solid and liquid phases. The schematic of the thermal model for the slab configuration is shown in Fig. 3. For the purposes of this paper, we are solely interested in the steady-state regression of the fuel slab. Namely, the velocity of the liquid-gas interface and the solid-liquid interface are assumed to be equal and constant. This, of course, implies that the thickness of the melt layer is also constant. For the sake of simplicity we further assume that the thermophysical properties of the material both in the liquid phase and also in the solid phase are uniform. The effect of convection in the liquid layer is also ignored because of the small melt layer thicknesses for which the Reynolds numbers are relatively small (a couple of hundreds) and the temperature gradients are fairly large.

In our analysis we have included the possibility of the penetration of the thermal radiation into the fuel slab. Several simplifying assumptions are introduced in the radiation treatment. First, the radiative flux field is assumed to be one-dimensional. Since the temperature levels in the slab are small, the contribution of radiation emitted by internal material to the radiative intensity is negligible. The absorbing character of both the liquid and also the solid material are assumed to behave like a gray body, namely the absorption coefficient is independent of the frequency of the radiation. Note that the absorption characteristics for typical hydrocarbons used in cryogenic hybrid applications, such as pentane, are reasonably flat in the medium IR range of the spectrum[8,9]. Even if this is not the case, the use of a constant absorption coefficient obtained by averaging over the band of the spectrum of the incoming radiation can be justified[11]. Furthermore the non-collimated effects of the incoming radiation to the fuel slab surface are neglected.

Under these simplifying assumptions the thermal analysis yields the following expression for the thickness of the melt layer[10].

$$h = -\delta_l \ln(\psi) \qquad (1a)$$

where the characteristic thermal thickness in the liquid phase is defined as $\delta_l = \kappa_l \rho_s / \dot{r} \rho_l$. The thickness parameter, ψ, which depends mainly on the thermophysical properties and radiative characteristics of the fuel and the nature of the heat transfer to the fuel surface can be found as a solution of the following nonlinear equation.

$$\psi = \frac{h_m(R_l - 1) + h_v(\dot{Q}_r/\dot{Q}_w)\ \psi^{R_l}}{h_e(R_l - 1) + h_v(\dot{Q}_r/\dot{Q}_w)} \qquad (1b)$$

Here the following definitions of the effective heating parameters are introduced for convenience.

$$h_m = L_m + C_s(T_m - T_a) \qquad (2a)$$

$$h_e = h_m + C_l(T_v - T_m) \qquad (2b)$$

$$h_v \equiv \frac{\dot{Q}_w}{\rho_s \dot{r}} = h_e + L_v(\dot{r}_v/\dot{r}) \qquad (2c)$$

The form of effective heat of gasification, h_v, given in Eq. 2c is slightly different than the expressions commonly encountered in the literature, since no heat is required to vaporize the material transported by means of entrainment.

Note that T_a, T_m, T_v are the initial, melting and vaporization temperatures of the fuel, respectively. $\dot{Q}_r$ and $\dot{Q}_w$ are the radiative and total heat fluxes to the fuel surface, C_l and C_s are the average specific heats of the liquid and solid and L_m and L_v are the latent heats for melting and vaporization. Also note that $\dot{r}$ and $\dot{r}_v$ are the total and vaporization components of the regression rate. Another important parameter that appears in the thickness expression is the nondimensional radiation parameter, R_l, which is defined as the ratio of the thermal thickness to the radiative thickness in the liquid phase.

$$R_l = \delta_l a_l \qquad (3)$$

Note that a_l is the average gray body absorption coefficient in the liquid phase.

An interesting observation is that, solid absorptivity does not appear in Eqs. 1a or 1b and the melt layer thickness is independent of the radiative characteristics of the solid material. This can be deduced from the fact that the only contribution of the solid-state temperature distribution on the thickness is through the heat transfer from the solid at the liquid-solid interface. It can be shown that the solid thermal profile in the neighborhood of the interface and thus the heat flux at the interface (from the solid side) is independent of the distribution of the radiative heating in the solid.

An explicit solution for the algebraic nonlinear equation, Eq. 1b, for the general case could not be obtained. We focus on the following two limiting cases of practical interest.

1) $R_l \gg 1$: The absorption of the radiation in the liquid layer is very large. In this extreme case of an opaque liquid layer, all the radiative heat is absorbed at the liquid-gas interface. The thickness can be solved explicitly as

$$h = \delta_l \ln\left[1 + C_l(T_v - T_m)/h_m\right]. \qquad (4)$$

Note that all the thermophysical properties of the fuel material are lumped in the logarithmic term and the $\dot{Q}_r/\dot{Q}_c$ ratio[§] does not affect the thickness. This case is important for propellants that are loaded with strongly absorbing materials such as carbon black.

2) $R_l \ll 1$: In this other extreme, the absorption of the radiation in the liquid phase is small. Here the thickness of the thermal layer in the liquid is much smaller than the radiative thickness in the liquid and as a consequence all the radiative flux is absorbed in the solid. The effect of the entrainment mass transfer on the thickness is also included in this formulation. Unlike the other extreme, in this case the film thickness depends on the ratio of the radiative heat flux to the convective heat flux and it can be expressed as

$$h = \delta_l \ln\left[1 + \frac{C_l(T_v - T_m)}{h_m - h_v(\dot{Q}_r/\dot{Q}_w)}\right]. \qquad (5)$$

Note that the dependence of the thickness on $\dot{r}_v/\dot{r}$ comes from the effective heat of gasification, h_v that appears explicitly in this formula and is defined in Eq. 2c. Note that an important common property of the regression rate expressions Eq. 4 and Eq. 5 is that the melt layer thickness is proportional to the characteristic thermal length of the liquid, δ_l, and thus inversely proportional to the regression rate ($h \propto 1/\dot{r}$).

As indicated by Eq. 1b, some knowledge of the order of magnitude of the liquid absoptivity parameter is essential for a reliable estimation of the melt layer thickness. We have calculated the average absorptivity of n-pentane using the published Near Infrared Region (NIR) and Middle Infrared Region (MIR) absorption spectra for this material[8,9]. In the calculations, we have assumed a continuous spectral distribution (according to Planck's Law) for the intensity of the impinging radiation from the combustion gases at an effective radiation temperature of 1800 K[11]. At this temperature the radiation peak takes place at a wave number of 6211 cm^{-1} and most of the heat transfer is in the Near Infrared Region of the spectrum. The estimated average absorption coefficient

---

[§] Note that $\dfrac{\dot{Q}_r}{\dot{Q}_w} = \dfrac{\dot{Q}_r/\dot{Q}_c}{1 + \dot{Q}_r/\dot{Q}_c}$ where $\dot{Q}_c$ is the convective heat flux to the fuel surface.

for pentane is $a_l = 1.62 \ mm^{-1}$ which results in $R_l = 0.13/\dot{r}$ (i.e. $\dot{r}$ is in mm/sec). For pure pentane at regression rate values larger than 1 mm/sec, which are typical for fast burning liquefying propellants, the liquid absoptivity can be ignored. Thus for all pentane melt layer thickness calculations presented in this paper, the approximate relation, Eq. 5, is used instead of the exact nonlinear relation, Eq. 1b.

One of the important parameters that affect the thickness of the melt layer is the ambient temperature of the fuel slab. Fig. 4 shows the plots of the melt layer thickness versus the regression rate for various ambient temperatures for a pentane fuel slab for $\dot{Q}_r/\dot{Q}_c = 0.1$ and $\dot{r}_v/\dot{r} = 0.5$. The material properties used in the calculations are given in Table 1. Note that an increase in the ambient temperature of the fuel slab results in an increase in the melt layer thickness. The maximum film thickness for a given regression rate is attained when the ambient temperature is equal to the melting temperature.

A plot of the variation of the film thickness with the relative radiative heat transfer, $\dot{Q}_r/\dot{Q}_c$, for a pentane system is shown in Fig. 5. The figure reveals the interesting phenomenon that at a critical value of the radiation factor (around 0.3 for pentane with 10 % entrainment), the steady-state film thickness grows indefinitely. This fact can be seen from Eq. 5, namely at the critical value of this factor the numerator of the argument of the logarithm diminishes. In physical terms, during this critical operation, the energy balance at the liquid-solid interface requires zero conductive heat transfer from the liquid side. This condition imposes a zero temperature gradient on the liquid side of the interface, which can only be achieved with an infinite thickness of the liquid layer. However the growth to large thicknesses can only be achieved in a long transient period, which cannot be estimated with our steady-state model. Fig. 5 also shows that the effect of entrainment mass transfer is to reduce the thickness at a given radiation factor and to increase the critical value of the radiation factor. This effect is generated from the entrainment regression rate dependence of the effective heat of gasification (Eq. 2c).

B) Linear Stability Investigation

The instability of the liquid film formed on the surface of a hybrid fuel grain is essential for the possibility of entrainment from the liquid interface. Although the stability of liquid layers are extensively studied in the past[12,13,14,15], the behavior of films under strong blowing conditions and relatively high liquid Reynolds numbers, which are encountered in hybrids, is not explored. In this section, we will summarize the linear stability investigation of a liquid layer with strong blowing under the effect of the strong shear force generated by the gas flow in the port. Details of the stability investigation are presented in Ref. 10.

The schematic of the liquid layer stability model is shown in Fig. 6. For simplicity, we ignore the effect of density variations and all chemical reactions in the gas phase on the stability. In the calculations we modify and adapt the linearized gas phase equations derived by Benjamin[16] for the incompressible flow over a wavy wall. Since our predictions for the Reynolds numbers for the hybrid liquid films are typically on the order of a couple of hundreds, both the small Reynolds number and also the high Reynolds number approximations[12,13] as the solution techniques for the film stability equation introduced in the literature are not satisfactory. For that reason we develop new solution techniques for the liquid layer aspect of the problem.

The body force, g, is taken in the normal direction in order to make direct comparison with the previous stability work reported in the literature[13]. Note that, for a spin stabilized rocket, the centrifugal acceleration will generate a body force in the normal direction acting outwards as indicated in Fig. 6. The effect of axial acceleration of a missile on the stability is not addressed in this paper. Since the melt layer thicknesses are very small for typical hybrid fuels, it is fair to state that for moderate accelerations, the effect of the axial body force on the stability is small compared to the dominant effect of the shear forces generated by the gas flow in the port.

As stated earlier, in our analysis we ignore the variations of the fluid properties across the thickness of the layer. We believe that the effect of these variations is small on the stability behavior of the film. We further assume that liquid flow in the melt layer is laminar in nature. This is a reasonable approximation for most hybrid melt layers, which are typically characterized with Reynolds numbers less than 300.

For a burning fuel slab, the base flow in the melt layer will be steady state only with respect to a coordinate frame moving with the burning surface. In this coordinate frame there will be a constant non-zero normal velocity component in the liquid layer which is induced by the density difference between the liquid and solid phases. The mass balance requires that this vertical velocity is

$$V_l = \dot{r}\rho_s/\rho_l. \qquad (6)$$

For the described flow field, the velocity component of the base flow parallel to the burning surface can be written as

$$U_o(y) = U_l^o \left[e^{b(y/h)} - 1 \right] / b e^b \qquad (7)$$

where the velocity at the liquid-gas interface, U_l^o and the liquid phase blowing parameter (or regression rate parameter), b are define as

$$U_l^o = \tau_g h / \mu_l \quad \text{and} \quad b \equiv \frac{V_l h \rho_l}{\mu_l} = \frac{\rho_s}{\rho_l} \frac{h}{\delta_m}.$$

Note that the momentum thickness for the liquid layer is defined as $\delta_m = \mu_l / \rho_l \dot{r}$. Here τ_g is the mean shear stress exerted on the liquid surface by the gas and μ_l is the liquid viscosity. For typical operating conditions of hybrids the liquid blowing parameter falls in the range of 0.1-1.0.

In the limit of zero liquid blowing ($\dot{r} = 0$), the application of the L'Hospital's rule yields the following linear velocity profile of the standard Couette flow as expected.

$$U_o(y) = U_l^o \, y / h = \tau_g y / \mu_l \qquad (8)$$

According to Eq. 7 the liquid velocity at the surface is

$$U_o(h) \equiv U_l = U_l^o \left[e^b - 1 \right] / b e^b. \qquad (9)$$

In Fig. 7 the plot of the velocity profiles according to Eq.7 and Eq. 8 are shown for a typical blowing parameter value of 0.4. It is apparent that the exact velocity profile is quite different from the simple Couette flow profile. However it is observed that for values of b smaller than 0.8, the exact solution is fairly close to a linear variation from the zero wall value to the maximum velocity predicted by Eq. 9. Note that the first order effect of the injection is to reduce the surface velocity of the liquid. For that reason the following corrected linear profile is a good approximation for small blowing parameters (i.e. See Fig. 7)

$$U_o(y) = U_l^o \frac{e^b - 1}{b e^b} \frac{y}{h} \qquad (10)$$

The corrected linear velocity profile given by Eq. 10 will be used in the linear stability investigations as an approximation for the base flow. This simplification is essential for the analytic development of an explicit stability expression for the film layer.

After perturbing the liquid flow field around the base flow presented in the previous paragraphs and assuming a general harmonic disturbance for the liquid-gas interface waveform, we obtain the following nondimensional Orr-Sommerfeld equation for the y-component of the perturbation stream function, ϕ.

$$\phi^{IV} - 2\alpha^2 \phi'' + \alpha^4 \phi - b\left(\phi''' - \alpha^2 \phi'\right) =$$
$$i\alpha \, \mathrm{Re}(\bar{y} - c)\left(\phi'' - \alpha^2 \phi\right) \qquad (11)$$

Here α is the nondimensional wave number and c is the nondimenional amplification parameter and Re is the liquid Reynolds number. Note that in Eq. 11 we have used the approximate mean velocity expression given by Eq. 10, which simplifies to $\bar{U}_o = \bar{y}$ in the nondimensional form. The extra term multiplied by b is due to the vertical motion of the liquid.

Next we consider the boundary conditions for the Orr-Sommerfeld equation. The first two of the boundary conditions can be obtained from the velocity requirements at the solid-liquid interface. The physical statement of the requirements are 1) The parallel component of the velocity at solid wall must be zero due to the no slip condition. 2) The regression rate of the slab is steady. These can be written in terms of the stream function formulation as

$$\phi(0) = 0 \quad \text{and} \quad \phi'(0) = 0. \qquad (12)$$

Another requirement that needs to be satisfied by the solution is the kinematic boundary condition at the liquid-gas interface. In the linear form this can be written as

$$\phi(1) = 1 - c. \qquad (13)$$

There are two other constraints that limit the possibility of solutions, which come from the dynamic conditions at the liquid-gas interface. These are the shear and the normal force balances at the liquid surface. The shear force balance in the linear form dictates

$$\frac{\bar{\tau}_g}{\eta} = -\frac{1}{\mathrm{Re}}\left(\phi''(1) + \alpha^2 \phi(1)\right). \qquad (14)$$

In this relation $\bar{\tau}_g$ is the nondimensional gas phase shear stress perturbation on the liquid interface. Note that the gas shear perturbation should be determined by solving the gas phase perturbation equations, which will be discussed later. For present purposes we consider $\bar{\tau}_g$ as a known input for the liquid layer stability problem.

Finally the normal force balance at the surface yields

$$(1-c)\phi'(1) - \phi(1) - \frac{1}{i\alpha \mathrm{Re}}\left[\phi'''(1) - b\phi''(1) - 3\alpha^2\phi'(1)\right] =$$

$$\left(\frac{\alpha^2}{We} + \frac{1}{Fr} - \frac{\bar{P}_g}{\eta}\right)\frac{\phi(1)}{1-c} \qquad (15)$$

Here $\bar{P}_g$ is the nondimensional gas phase pressure perturbation on the liquid surface, We is the Weber number and Fr is the Froude number where σ is the surface tension.

$$We = \frac{\rho h U_l}{\sigma} \quad \text{and} \quad Fr = \frac{U_l^2}{gh} \qquad (16)$$

Eqs. 12, 13, 14 and 15 set five conditions on the fourth order differential equation, Eq. 11. Thus this is an overposed boundary value problem. The correct approach is to consider the Orr-Sommerfeld equation with those five conditions as an eigenvalue problem, the eigenvalue being the amplification parameter, c. The direct numerical solution of this eigenvalue problem is computationally expensive, since it requires many iterations (each iteration is a finite difference solution itself) for every selection of the parameters such as the Reynolds number, Froude number or the Weber number that might effect the stability of the layer. For that reason it is desirable to develop analytical solutions.

We have obtained solutions for the presented stability problem by using two independent techniques. We first developed a power series solution that can only be applied to films with Reynolds numbers less than unity. For the power series solution, we modified Craik's technique[13], which was originally applied to a simpler case of a layer with no blowing. Since in hybrid applications the film layer Reynolds numbers can be significantly larger than unity, we also formulated an exact solution for the liquid stability problem defined above.

For the purposes of this paper, we will only present the exact solution developed in great detail in Ref. 10.

$$\phi(\bar{y}) = \sum_{n=1}^{4} c_n \phi_n(\bar{y}) \qquad (17)$$

The four independent particular solutions of the Orr-Sommerfeld equation are

$$\phi_1 = e^{\alpha \bar{y}} \qquad (18a)$$

$$\phi_2 = e^{-\alpha \bar{y}} \qquad (18b)$$

$$\phi_3(\bar{y}) = \frac{1}{\alpha}\int_{\bar{y}_o}^{\bar{y}} \sinh\left[\alpha(\bar{y}-\hat{y})\right]e^{-(\tilde{B}/2)\tilde{z}(\hat{y})}Ai\left[\tilde{z}(\hat{y}) + \tilde{B}^2/4\right]d\hat{y}$$

$$\qquad (18c)$$

$$\phi_4(\bar{y}) = \frac{1}{\alpha}\int_{\bar{y}_o}^{\bar{y}} \sinh\left[\alpha(\bar{y}-\hat{y})\right]e^{-(\tilde{B}/2)\tilde{z}(\hat{y})}Bi\left[\tilde{z}(\hat{y}) + \tilde{B}^2/4\right]d\hat{y}$$

$$\qquad (18d)$$

where

$$\tilde{z} = -\frac{\alpha^2 + i\alpha\mathrm{Re}(\bar{y}-c)}{(\alpha\mathrm{Re})^{2/3}} \quad \text{and} \quad \tilde{B} = -ib/(\alpha\mathrm{Re})^{1/3}.$$

These boundary conditions with the analytical expressions for the independent solutions can now be used to solve the eigenvalue problem for the eigenvalue c. It is important to note that the selection of $\bar{y}_o = 0$ significantly simplifies the solution since the first two of the boundary conditions require $c_1 = c_2 = 0$ and drop out of the system. In this case the system is reduced to three equations for three unknowns, c_3, c_4, c. Note that even the reduced system involves difficult integrals and it is nonlinear in c. Thus the solution requires numerical integration and some iterative procedure on c. In order to perform the calculations, we developed a MATHEMATICA program that automates the solution procedure and iteratively solves the eigenvalue c, for any given selection of parameters. The time required for the solution at a specified point of the parameter space is less than a second with a modern desktop computer. Thus the analytic solution developed for the film stability problem is apparently very efficient in terms of the computation time over the numerical simulation of the Orr-Somerfeld equation or the Navier-Stokes equations.

The linear stability problem discussed in the previous paragraphs requires the gas phase response as the input. Here we will describe the gas phase perturbation treatment that was first developed by Benjamin[16] and later adapted to the thin film stability problem by Craik[13]. Benjamin investigated the flow field generated by a shearing gas flow on a wavy surface and presented explicit formulas for the shear and normal stresses disturbances induced by the shear flow on the surface. The following fundamental simplifications were introduced in the treatment.

- The primary gas flow is parallel and in the direction of the surface waves.
- In the case of a turbulent gas flow, the interactions with the turbulence and the wave motion are neglected. In other words, the mean velocity distribution for the turbulent case is disturbed by

8

the waves in the same fashion as the velocity distribution in an equivalent laminar flow.

- The complete solution for the Orr-Sommerfeld equation derived for the gas phase is expressed as a sum of the inviscid solution, $\psi_g(\zeta)$ and a viscous solution confined to a small thickness next to the surface, $f_g(\zeta)$, where ζ is the curvilinear coordinate that is perpendicular to the wavy surface. The viscous solution, which rapidly diminishes as one moves away from the surface, is required to satisfy the wall boundary conditions imposed on the fourth order Orr-Sommerfeld equation. The region where $f_g(\zeta)$ is significant compared to the inviscid solution is named as the "wall friction layer", not to be confused with the viscous sublayer of a turbulent boundary layer.

The explicit solution for the shear stress and pressure perturbations presented by Benjamin is revised and reformulated by Craik in the context of the liquid layer stability problem formulated earlier in this paper. We have discovered that the simplifying assumption, $\Delta \ll 1$, that was used by both Benjamin and Craik significantly restricts the applicability of the gas phase stress perturbation expressions given in Refs. 13 and 16. This assumption on Δ is particularly invalid for hybrid rocket applications, typically characterized by high gas velocities and small disturbance wave lengths. We followed Benjamin's original derivation to refine the set of gas phase stress perturbation formulas by relaxing the restricting assumption on Δ. We found that the nondimensional normal and the tangential stress perturbations $\bar{P}_g$ and $\bar{\tau}_g$ which are valid for any value of Δ can be approximated by the following equations.

$$\frac{\bar{P}_g}{\eta} = \frac{(\alpha/\mathrm{Re})}{1 + 1.288\ e^{i\pi/6}\Delta}\left[\frac{I}{C_f} - 2i\right] \qquad (19a)$$

$$\frac{\bar{\tau}_g}{\eta} = 1.373\ \left(\mu_l/\mu_g\right)^{2/3}\left(\rho_g/\rho_l\right)\left(I/c_f\right)\frac{e^{i\pi/3}\alpha^3(\alpha\,\mathrm{Re})^{-4/3}}{\left(1 + 1.288\ e^{i\pi/6}\Delta\right)^2}$$

$$(19b)$$

$$\Delta = \left(I/C_f\right)\left(\mu_g/\mu_l\right)^{4/3}\left(\rho_l/\rho_g\right)^{2/3}(\alpha\,\mathrm{Re})^{-2/3}\alpha^2 \quad (19c)$$

$$I = \int_0^{\infty}\left(U_g/U_g^o\right)^2 e^{-\alpha\zeta}d(\alpha\zeta) \qquad (19d)$$

Here U_g is the mean boundary layer velocity profile of the gas flow, U_g^o is the gas velocity at the center of the port and μ_g, ρ_g are the average viscosity and the density of the gas in the port, respectively. The real parts of stress parameters correspond to the components of stress that are in phase with the wave displacement, whereas the imaginary parts of the stress parameters represent the stress components, which are in phase with the wave slope.

For the sake of simplicity, the following form of the gas phase velocity profile will be used in evaluating the integral, I.

$$\frac{U_g(\zeta)}{U_g^o} = \left(\frac{2\ \zeta\ h}{d_p}\right)^{1/7} \quad \text{for}\quad \zeta < d_p/2h \qquad (20a)$$

$$\frac{U_g(\zeta)}{U_g^o} = \left(2 - \frac{2\ \zeta\ h}{d_p}\right)^{1/7} \quad \text{for}\quad d_p/2h < \zeta < d_p/h \qquad (20b)$$

Note that for hybrid rocket applications, the boundaries of the integral in Eq. 19d need to be from 0 to d_p/h.

Finally, it can be shown that with use of the shear balance at the liquid gas interface, the liquid layer Reynolds number can be written in terms of the gas flow parameters and the properties of the liquid.

$$\mathrm{Re} = \mathrm{Re}_g^2\ c_f\ \frac{\rho_l}{\rho_g}\left(\frac{\mu_g}{\mu_l}\right)^2\left(\frac{h}{z}\right)^2\frac{e^b - 1}{b\ e^b} \qquad (21)$$

Here Re_g is the gas phase Reynolds number, z is the axial distance in the port, c_f is the skin friction coefficient.

In the following paragraphs we present the results for the liquid layer stability problem that are obtained with the application of the solution techniques discussed in the previous section. For all of the calculations that will be conducted in this paper, the following geometrical and gas phase properties will be used.

$$d_p = 2\ cm, \quad z = 14\ cm$$

$$\mu_g = 6.5\ 10^{-6}\ N\sec, \quad \rho_g = 8\ kg/m^3$$

Liquid properties for various materials are listed in Table 1. The solid densities of all the cryogenic propellants are assumed to be equal to the density of solid pentane, 850 kg/m³. The solid density of the wax is taken to be 930 kg/m³. The gas phase blowing parameter, B, used in the calculations for all the fuels is 7.

One of the most interesting results of this linear theory is that even at very small film thicknesses there exists a finite range of amplified wave numbers, namely the layer is unstable over a finite range of wave numbers. The instabilities of that type were first discovered for thin water films in a wind tunnel by Craik[13] and they are called the "slow waves". These are generated by the interaction of the gas phase shear stresses acting on the liquid surface with the slope of the liquid layer surface. Fig. 8 shows a typical form of the dimensional amplification rate of the interface disturbance, $-\left(\mu_l/h^2\rho_l\right)\mathrm{Im}(c\alpha\,\mathrm{Re})$, as a function of the dimensional wave number, $k=\alpha\,h$, calculated with use of the linear stability theory outlined in this paper. For this calculation, the liquid is water, liquid Reynolds number is 50, film thickness is 0.3 mm, regression rate is zero and the Froude number corresponding to the body force of 9.81 m/sec^2 is 9.458. As indicated in the figure, there is a positive amplification domain, which lies between two cutoff wave numbers. The amplification takes a maximum value at a wave number between these two cutoff wave numbers. This is the most amplified wave number and the corresponding wavelength is expected to be the observed size of the disturbance in the actual flow system. As the body force diminishes the first cutoff point moves towards zero.

Intuitively, the most important parameter that links the linear stability results to the entrainment rate of the liquid from the surface is the amplification rate of the disturbances. Fig. 9 shows the effect of the liquid Reynolds number on the amplification curves. This plot is for a 0.3 mm thick pentane film. The liquid Reynolds number is adjusted by changing the port mass flux from 42.7 kg/m^2-sec to 92.2 kg/m^2-sec. The regression rate parameter is 0.55 and the body force is assumed to be zero. Note that as the liquid layer Reynolds number (which is directly proportional to the gas stream dynamic pressure) increases, the amplification rate increases. The Reynolds number also increases the most amplified wave number, meaning that at higher gas flow velocities the expected wavelengths of the instabilities are smaller. This latter result is in good agreement with the experimental findings for the scale of waves formed on the surface of a thin film[17].

The effect of the liquid injection on the film stability is shown in Fig. 10. The amplification rate as a function of the wave number for three values of regression rate parameter, b, is calculated with use of the exact solution. This case is for a 0.15 mm pentane film with a liquid Reynolds number of 50 and a Froude number of zero. Fig. 10 shows that the normal liquid injection has a slight stabilizing effect on the film. This

conclusion is also confirmed by the power series solution. For a situation for which the mass flux is kept constant rather than the liquid Reynolds number, the effect of the regression rate parameter will be more dominant. This is due to the fact that, according to Eq. 52, an increase in the regression rate parameter decreases the liquid Reynolds number for a given port mass flux value.

Another very important result that came out of the stability investigation is that both the surface tension and also the viscosity of the liquid have a stabilizing effect on the liquid film. It turns out that this feature of the thin film instabilities plays a major role in determining which propellant is likely to sustain instabilities and potentially entrain droplets into the gas stream. In order to demonstrate the effect of material properties on the stability, the amplification curves for various liquids at a fixed film thickness of 0.15 mm are shown in Fig. 11. For all the liquids the regression rate is 1 mm/sec and the port mass flux is 80 kg/m^2-sec. Note that liquids with higher viscosities such as isopropanol and HFI are more stable than the liquids with small viscosity values. The stability curve for one grade paraffin wax, which is solid under ambient conditions, is included in the figure. It is predicted by the theory that this particular grade of wax would form an unstable melt layer promoting entrainment of liquid droplets into the gas stream.

As a final note of this section we like to state that the linear stability theory presented in this paper can also be applied to classical hybrid propellants that form a liquid layer on their burning surfaces. One such propellant is HDPE (high-density polyethylene) polymer, which has been tested extensively as a hybrid fuel. In Ref.10 it is shown that the melt layer of HDPE is 4 orders of magnitude more viscous than pentane. The linear theory suggests that the melt layers of these highly viscous polymeric fuels will be extremely stable at the port mass flux levels typically encountered in hybrid motors.

C) Liquid Entrainment Relationships

The linear stability treatment outlined in the previous section revealed that the melt layers typically encountered in hybrid applications could develop interfacial instabilities. Even though the existence of these linear instabilities is a necessary condition, it is not sufficient for the entrainment process to occur. Before entrainment of droplets can take place, the infinitesimal harmonic disturbances growing at the liquid-gas interface must grow into a non-harmonic waveform with a finite amplitude. The process of growth to a finite amplitude and eventually entrainment of droplets is a highly nonlinear phenomenon, which is

extremely difficult to model. We bypass this difficult but critical step by using some emprical relations that are introduced in the existing literature for the entrainment from thin liquid films under strong shear forces exerted by a gas flow. As stated in the literature, one plausible mechanism for droplet entrainment from these thin films at large Reynolds numbers is through the formation of nonlinear "Roll Waves". As schematically indicated in Fig. 2, the droplets are drawn from the tips of these nonlinear waves by the stresses exerted by the local gas flow.

The most relevant experimental work on entrainment is reported by Gater and L'Ecuyer in an early paper[17]. In this study which was motivated to address the liquid injection requirements for film cooling applications, the entrainment rates from thin films of various liquids (including some hydrocarbons such as RP-1, methanol) under strong gas flow were measured. The experiments were performed in a wind tunnel and some tests were executed with hot gas flow. The entrainment relationship suggested by Gater and L'Ecuyer, which is slightly modified in Ref. 10 can be written as

$$\dot{m}_{ent} = \rho_l \dot{r}_{ent} = 1.41\ 10^{-3} \left(X_e - 2109 \right) \dot{m}_l. \quad (22)$$

Here is $\dot{r}_{ent}$ the entrainment portion of the regression rate. The entrainment parameter, X_e and the liquid flow rate per unit width in the melt layer, $\dot{m}_l$, can be written as

$$X_e = \frac{P_d^{0.5}}{\sigma} \left(\frac{T_g}{T_v} \right)^{0.25} \text{ and } \dot{m}_l = \frac{P_d c_f h^2 \rho_l}{2\mu_l}. \quad (23)$$

Note that P_g is the dynamic pressure of the gas flow ($P_g = G^2/\rho_g$) and T_g is the gas stream average temperature. The temperature ratio is included as a correction for the density variation in the gas.

In the nuclear reactor field there has been significant research on the entrainment mass transfer[18,19], since it has importance in the emergency cooling of the reactors. Various models for entrainment are developed at different regimes of operation. In general, the experimental findings of those studies also confirm the results previously mentioned. However the form of dependence of the entrainment mass transfer on the parameters is somewhat different in every study. Thus it is fair to state that the proper form of scaling for the entrainment still needs to be resolved.

In the light of experimental findings and the results of the linear theory, we suggest the following

general empirical expression (for operation sufficiently remote from the critical conditions for entrainment) for the entrainment rate of liquid droplets in terms of the relevant properties of the hybrid motor.

$$\dot{m}_{ent} \propto P_d^{\hat{\alpha}} h^{\hat{\beta}} \big/ \mu_l^{\hat{\gamma}} \sigma^{\hat{\pi}} \quad (24)$$

The experimental data and the linear stability theory suggest that the dynamic pressure exponent is expected to be in the range of 1-1.5. For example Gater and L'Ecuyer[17] scaling for large mass fluxes indicates that $\hat{\alpha}$ is approximately 1.5 and $\hat{\beta}$ is equal to 2. The viscosity and surface tension exponents are both predicted to be 1. The series of entrainment relations given by Nigmatulin et al[18] suggest a weaker dependence on both the dynamic pressure and also the thickness ($\hat{\alpha} = 1$ and $\hat{\beta} = 1$). The scaling with respect to the material properties is not estimated accurately by the entrainment relations given by Nigmatulin, since mainly water data was considered in the study. We believe that under the conditions of hybrid rocket applications, the melt layer viscosity plays a more important role compared to the surface tension in establishing the entrainment mass transfer rate (i.e. $\hat{\gamma} > \hat{\pi}$).

A very useful empirical relation for the critical conditions for the onset of entrainment given by Ref. 20 is rearranged here in terms of the practical conditions in the motor.

$$G^{1.6} h^{0.6} \geq 2.5\ 10^{-3} \frac{1}{c_f^{0.8}} \frac{\rho_g^{1.3}}{\rho_l^{0.3}} \frac{\mu_l^{0.6}\sigma}{\mu_g} \quad (25)$$

Note that this relation only holds for a laminar film (Re<300). Unlike the entrainment relations this formula has the correct scaling with the material properties of the liquid. Fig. 12 shows the plot of the entrainment boundary for various liquid materials in the mass flux film thickness plane (See Table 1 for the material properties used in calculations). Note that for each liquid, the entrainment takes place in the region above the curve.

D) Modification of the Classical Theory for Entrainment

It has been shown in the previous sections that a liquid layer can be formed on the fuel grain and this liquid layer can be unstable over a reasonable range of parameters typical of hybrid operation. It is also indicated that the instabilities in the liquid layer may induce the entrainment of liquid droplets into the gas

11

stream. The final phase of the development involves the modification of the classical hybrid boundary layer combustion theory for the possibility of entrainment mass transfer from the fuel grain.

The formation of the liquid layer instabilities and entrainment of liquid droplets require three major modifications in the classical hybrid combustion theory.

- The ratio of the enthalpy difference to the effective heat of gasification ($\Delta h/h_v$) that appears in the thermal blowing parameter expression is altered. The effective heat of gasification is reduced since the evaporation energy required for the fuel mass transfer from the surface is partly avoided by the mechanical entrainment of the liquid. Whereas, the enthalpy difference between the flame and the surface is also reduced, since some of the reactants are now in liquid phase. It is estimated that, the reduction in the effective heat of gasification is more dominant than the change in the enthalpy difference. Thus as a first approximation we assume that the reduction in the flame enthalpy is negligible.

- The blocking factor, C_H/C_{Ho}, that modifies the convective heat flux to the surface is also altered due to the presence of the two-phase flow. As a first approximation we ignore the effect of the liquid droplets on the momentum and energy transfer. Under this assumption the blocking factor can be expressed as a function of evaporation blowing parameter.

$$C_H/C_{Ho} = f(B_g)$$

The evaporation blowing parameter, B_g, includes only the gaseous phase mass transfer from the fuel surface. We assume that evaporation of the droplets released from the liquid surface into the gas stream does not take place beneath the flame sheet. This assumption is consistent with the flame sheet approximation, which is a standard one in hybrid combustion modeling. Moreover, it is a reasonable approximation for typical hybrid operating conditions that are characterized by high blowing rates and thus low residence time of droplets between the liquid surface and the diffusion flame. However, we believe that a more rigorous treatment of the two-phase flow in the hybrid boundary layer will be an important step in the further improvement of the liquefying hybrid theory.

- The ripples formed on the liquid layer surface increase the surface roughness and the heat transfer from the flame front to the surface.

In general, the total regression rate of a hybrid motor can be written as a sum of the evaporation regression rate that is generated by the vaporization of the liquid into the gas stream and the entrainment regression rate, which is related to the mass transfer mechanically extracted from the liquid surface.

$$\dot{r} = \dot{r}_v + \dot{r}_{ent} \qquad (26)$$

For an arbitrary combination of the entrainment and evaporative mass transfer the energy balance at the liquid gas interface is

$$\dot{r}_v + \left[R_{he} + R_{hv}(\dot{r}_v/\dot{r})\right]\dot{r}_{ent} =$$
$$F_r \frac{0.03\mu_g^{0.2}}{\rho_f}(1+\dot{Q}_r/\dot{Q}_c)B\frac{C_H}{C_{Ho}}G^{0.8}z^{-0.2} \qquad (27)$$

where

$$R_{hv} = \frac{C_l\Delta T_l}{h_e+L_v} \quad \text{and} \quad R_{he} = \frac{h_m}{h_e+L_v}. \qquad (28)$$

Here the nondimensional energy parameters for entrainment (R_{he}) and vaporization (R_{hv}) are introduced because the material that is extracted through the entrainment mechanism possesses different heating histories (i.e. no heat of vaporization is required for entrainment). We postulate that the effective heating in the liquid phase required for fuel material which is going through the entrainment mass transfer mechanism reduces linearly as the vaporization component of the regression rate decreases. This extra complexity, which was ignored in the thickness estimation arguments, is introduced to capture the asymptotic behavior of regression rate in the entrainment-dominated region of operation. We would like to note that the effect of reduced liquid phase heating on the thickness at moderate entrainment conditions is very small since the thickness presents a logarithmic dependence on the energy terms.

The roughness parameter, F_r, is introduced in the energy equation to account for the increased heat transfer by wrinkling of the liquid surface. It has been argued by Gater and L'Ecuyer[17] that the surface roughness decreases with increasing dynamic pressure of the gas flow. This argument is based on the observed reduction in the scale of the interface disturbances with increasing dynamic pressure. Note that this phenomenon is captured by the linear theory which

shows decreasing wave length with increasing gas mass flux. The empirical formula for the roughness correction parameter suggested by Gater and L'Ecuyer can be expressed in terms of the operational parameters of the motor as

$$F_r = 1 + \frac{14.1\, \rho_g^{0.4}}{G^{0.8}\left(T_g/T_v\right)^{0.2}}.$$ (29)

In this formula the units of mass flux and gas density are kg/m²-sec and kg/m³, respectively.

We developed a new curve fit expression for the blowing correction, C_H/C_{Ho}, which is a reasonable approximation for the analytical expression given by Marxman[21] for a wide B_g range of 0-14 (See Fig. 13).

$$\frac{C_H}{C_{Ho}} \cong \frac{2}{2 + 1.25 B_g^{0.75}} = \frac{C_{B1}}{C_{B1} + C_{B2}\left(\dot{r}_v/\dot{r}_{cl}\right)^{0.75}}$$ (30)

Here the coefficients are defined as

$$C_{B1} \equiv \frac{2}{2 + 1.25 B^{0.75}} \quad \text{and} \quad C_{B2} \equiv \frac{1.25 B^{0.75}}{2 + 1.25 B^{0.75}}.$$

It is not acceptable to adapt one of the forms that are commonly used in the hybrid literature[1] (i.e. $C_H/C_{Ho} = B^{-0.68}$) in this study in which accuracy at low B values is essential. Classical expressions predict unrealistically large blocking factors (even larger than one) for B values close to zero. Note that B is the classical blowing parameter and $\dot{r}_{cl}$ is the classical regression rate of the system in the case of no entrainment. The classical regression rate can be written as

$$\dot{r}_{cl} = \frac{0.03 \mu_g^{0.2}}{\rho_f}\left(1 + \dot{Q}_r/\dot{Q}_c\right) B\, C_{B1} G^{0.8} z^{-0.2}.$$ (31)

Following the arguments in the proceeding section (i.e. Eq. 24) the entrainment regression rate can be expressed in terms of the mass flux in the port and the total regression rate.

$$\dot{r}_{ent} = a_{ent}\frac{G^{2\hat{\alpha}}}{\dot{r}^{\hat{\beta}}}$$ (32)

Here we used the definition of the dynamic pressure ($P_d = G^2/\rho_g$) and Eq. 4 or Eq. 5 for the film thickness expression. The entrainment parameter, a_{ent}, is a function of the properties of the selected propellant and

average gas density (ρ_g) in the chamber. For simplicity, we will assume that a_{ent} is constant for a given propellant.

Eqs. 26, 27, 28, 29 and 32 together with the blowing correction expression, Eq. 30, form a nonlinear set of algebraic equations which can be solved for a given propellant combination to obtain the total regression rate as a function of the axial location and local mass flux.

E) Application to Cryogenic Hybrid Rockets

For pentane as the frozen fuel, the regression rates are calculated iteratively from this nonlinear set of equations as a function of the mean mass flux in the port. Fig. 14 shows both the predicted regression rates and also the reduced instantaneous regression rate data for several pentane runs[10]. In the calculations $\hat{\alpha} = 1.5$, $\hat{\beta} = 1.5$, $a_{ent} = 8\ 10^{-14}$ (m$^{8.5}$sec$^{0.5}$/kg^3), $\dot{Q}_r/\dot{Q}_c = 0.15$, $z = 0.075$ (m), $\rho_g = 4$ (kg/m³), and $\mu_g = 6.5\ 10^{-5}$ (N-sec/m²) numerical values are used. The estimated blowing parameter value of 13.5 for the pentane-oxygen system is used in the calculations. The figure shows that the high regression rates observed in the pentane tests can be explained in the context of the liquid layer combustion theory. Most of the increase in the burning rate comes from the entrainment of droplets; reduced effective heat of gasification and reduced blocking correction. The roughness effect, however, accounts for a smaller increase in regression rates (i.e. increase in the surface heat transfer ranges from 30 % at low mass fluxes down to 5 % at the higher flux levels).

It is useful to obtain an upper limit for the regression rate of a hybrid fuel forming a liquid layer. In the extreme case the vaporization from the liquid surface is negligible, namely all the mass is transferred to the gas flow in the form of droplets. This upper bound can be quantitatively determined upon the consideration of Eq. 27. The maximum regression rate occurs when no vaporization at the surface takes place. Under the assumptions of our theory, for this extreme case, the blocking factor becomes unity. The maximum regression rate normalized with the classical value of the regression rate, for which no entrainment from the surface is allowed, becomes

$$\frac{\dot{r}_{\max}}{\dot{r}_{cl}} = \frac{1}{C_{B1} R_{he}}.$$ (33)

For pentane fuel the maximum regression rate is estimated to be approximately 23 times the classical

regression rate. Note that for pentane calculations the blowing parameter value of 13.5 and R_{he} value of 0.23 are used. This large upper limit for the amplification explains the experimentally observed regression rates that are determined to be 2-5 times larger than the expected (classical) values.

As shown in Table 1 and Fig. 1 some cryogenic hydrocarbons such as pentane, acetone and 2,2,5 tmh burn fast whereas some others such as isopropanol and HFI burn considerably more slowly. This observation can also be explained within the context of the liquid layer hybrid theory described in this paper. Fig. 12 shows the entrainment onset boundary for various propellants generated with use of Eq. 25. The parameter values of $\rho_g = 4\,(\mathrm{kg/m}^3)$, $c_f = 0.004$ and $\mu_g = 6.5\ 10^{-5}$ (N-sec/m^2) are used in the calculations. It is clear that isopropanol and HFI, which are much more viscous compared to the other materials, require large thresholds for entrainment. In order to reinforce this finding, we have used the scaling law, Eq. 24, to estimate the entrainment rates for given mass flux and film thickness for various materials. The entrainment rates are then reduced to entrainment parameters by normalizing with the entrainment rate for the reference propellant pentane. Calculations are performed with use of the viscosity and surface tension exponents of 1 and 0.7, respectively. The relative entrainment parameters are shown in Table 1. Clearly, the entrainment parameters of the viscous propellants (i.e. isopropanol, HFI) are one order of magnitude smaller than the other propellants. This finding reveals viscosity as a determining parameter controlling the burning rate of a liquefying hybrid propellant. In fact, viscosity of the imbedded propellant can be adjusted to tailor the regression rate of a hybrid rocket during the course of its operation. Moreover it can be stated that oxygen, which is an interesting alternative solid cryogenic hybrid propellant, is also predicted to be a fast burning material due to its low viscosity. This result is confirmed by the tests performed by ORBITEC[6].

Another important practical issue for the prediction of the performance of a propellant is its susceptivity to bulk heating by radiation penetrated through the slab. Specifically, it can be stated that the materials, which have small radiative absorptivities in their solid phases, potentially burn in an uncontrolled fashion. This is due to the possibility of sloughing of the propellant that is internally heated. In order to investigate this, we have estimated the outer web temperature as a function of the remaining web thickness for a typical pentane run[10]. It can be shown that, for pentane tests, the outer web temperature

changes very little until the last portion of the run after which it increases rapidly. Note that in the last third of the run the chamber pressure drops suddenly for the same test. This observation supports the possibility of sloughing due to bulk heating of the propellant. The extent of this uncontrolled operation mode over the whole burn time is expected to be more significant for propellants with smaller absorptivities of radiation. In fact for a propellant to be practical its absorptivity must be increased over a minimum value by possibly adding materials that are good absorbers of radiation (i.e. carbon black).

4) Paraffin Based Hybrid Rocket Fuel Test Results

Even though the liquid layer combustion theory is first developed to explain the burning behavior of solid cryogenic propellants, it is applicable to any material that would form a liquid layer on its burning surface.

In fact we have applied the theory to formulate a noncryogenic fast burning paraffin-based hybrid rocket fuel, SP-1. The entrainment onset boundary and the relative entrainment rate for the paraffin-based fuel are shown in Fig. 12 and Table 1, respectively. Surprisingly, the plot and table indicate that the predicted entrainment rate for this formulation is comparable to that of a low molecular weight cryogenic material such as pentane.

Experiments conducted with gaseous oxygen at Stanford University confirm the theory predictions on the paraffin-based fuel[22]. The burning rate of the fuel formulation SP-1 as a function of mass flux is approximately 3 times faster than the burning rates of HTPB as indicated by Fig. 15. Note that the average oxidizer mass flux is calculated based on the average port diameter.

This new fuel formulation delivers very high burning rates without compromising any of the advantages of the hybrid fuels. We believe that paraffin-based propellants may very well play a central role in the development of the hybrid rocket technology into operational propulsion systems.

Some of the key characteristics of the experimental setup used in the tests can summarized as follows (i.e. See Ref. 10 for a detailed description of the facility).

- Oxidizer is gaseous oxygen.
- Motor OD is 3 1/4".
- Initial fuel port diameter used in the tests ranges from 0.5" to 1.2".
- Oxidizer flow rate is set by a choked sonic orifice.
- Motor is ignited with a methane/Gox torch.

14

- Sonic orifice upstream pressure is measured to be used in the oxygen mass flow calculations. The chamber pressure is measured at the fore end of the motor.
- ATJ graphite is the material used for the nozzle and combustion chamber insulation.

The liquid layer hybrid combustion theory also covers the classical propellants that form a liquid layer. The reason that the classical polymeric propellants such HDPE do not burn fast (even though they might form a liquid layer) is their highly viscous melt layers. For example, the melt layer viscosity of HDPE is predicted[10] to be 4 orders of magnitude larger than the melt viscosity of pentane or wax. Naturally, at these super high viscosities, even at very high mass flux levels, the onset of entrainment is not achieved.

5) Conclusions

- In this paper the hybrid diffusion limited theory is generalized to hybrid fuels that burn by forming a liquid layer. In the first step of our development, we determined the conditions required to form a melt layer with a thickness sufficient to produce entrainment. It is shown that the melt layer thickness can be a few hundred microns thick for typical hybrid operating conditions. Next we have showed that these thin films with strong blowing could be unstable under hybrid operating conditions. Results reported in the literature are used to infer that the instabilities will result in the entrainment of droplets into the gas stream.
- It is determined that both the surface tension and the melt layer viscosity play a critical role in determining the entrainment characteristics of a material. It can be stated that materials with low viscosity and low surface tension will generate more entrainment. This fact explains why some of the classical fuels that form a melt layer (i.e. HDPE) do not generate high regression rates.
- The extra mass transfer mechanism can potentially increase the regression rates an order of magnitude larger than the estimated rates from the classical theory. This is mainly due to the reduced effective heat of gasification, decreased blocking factor in the hybrid boundary layer and higher heat transfer as a result of the increased surface roughness.
- The cryogenic hybrid rocket tests revealed regression rates 2-5 times larger than the expected rates estimated from the classical theory for low viscosity propellants such as pentane. The extended theory developed here successfully predicts these very high regression rates observed in the cryogenic tests. The liquid layer theory also explains the slow burning rates of high viscosity propellants.
- The application of the theory is not limited to solid cryogenic hybrid fuels. In fact we used our model to formulate a paraffin-based fuel which would exhibit high regression rates comparable to pentane. Tests at Stanford on a laboratory scale motor confirmed the predicted high regression rates for this fuel. The new paraffin-based materials comprise a class of fast burning non-cryogenic hybrid fuels with a wide spectrum of properties. This provides the opportunity to satisfy a broad range of mission requirements for the next generation of hybrid rockets.

6) Acknowledgments

7) References

[1]Marxman, G. A., Wooldridge, C. E., and Muzzy, R. J. "Fundamentals of Hybrid Boundary Combustion", Progress in Astronautics and Aeronautics, Vol.15, 1964 p 485.

[2]Larson, C. W., Pfeil, K. L., DeRose, M. E. and Carric, P. G., "High Pressure Combustion of Cryogenic Solid Fuels for Hybrid Rockets", AIAA paper No. 96-2594, AIAA/SAE/ASME/ASEE 32 nd Joint Propulsion Conference and Exhibit, July 1996.

[3]Larson, C. W., DeRose, M. E., Pfeil, K. L. and Carric, P. G. "High Pressure Combustion of Cryogenic Hybrid Fuels in a Lab-Scale Burner", Proccedings of the 1996 JANNAF Joint Propulsion Conference, Albuquerque, NM, December 9-13, 1996, published by CPIA, John Hopkins University.

[4]DeRose, M. E., Pfeil, K. L., Carric, P. G., and Larson, C. W. "Tube Burner Studies of Cryogenic Solid Combustion", AIAA paper No. 97-3076, AIAA/SAE/ASME/ASEE 33 rd Joint Propulsion Conference and Exhibit, July 1997.

[5]Gramer, D., Rice, E., Knuth, W. and Clair, C. St., "Experimental Investigation of a Metallized Cryogenic Hybrid Rocket Engine", AIAA paper No. 98-3509, AIAA/SAE/ASME/ASEE 34th Joint Propulsion Conference and Exhibit, July 1998.

[6]Clair, C. St., Rice, E., Knuth, W., and Gramer, D., "Advanced Cryogenic Solid Hybrid Rocket Engine Developments: Concept and Testing", AIAA paper No. 98-3508, AIAA/SAE/ASME/ASEE 34th Joint Propulsion Conference and Exhibit, July 1998.

[7]Estey, P., Altman, D. and McFarlane, J., "An Evaluation of Scaling Effects for Hybrid Rocket Motors", AIAA paper No. 91-2517, 1991.

[8]Lang, L. "Absorption Spectra in the Infrared Region", London Butterworths, 1974.

[9]Bentley, F. F., Smithson, L. D. and Rozek, A. L. "Infrared Spectra and Characteristic Frequencies ~700-300 cm -1", Interscience Publishers, 1968.

[10]Karabeyoglu, M. A., "Transient Combustion in Hybrid Rockets", Ph. D. Thesis, Stanford University, August 1998.

[11]Seigel, R. and Homel, J. R. "Thermal Radiation Heat Transfer", Hemisplane Publishing Coorporation, 1992.

[12]Schlichting, H., "Boundary Layer Theory", McGraw Hill, 1955.

[13]Craik, A. D. D., "Wind Generated Waves in Thin Liquid Films", *Journal of Fluid Mechanics*, vol. 26, part 2, pp. 369-392, 1966.

[14]Chang, I-Dee and Russel, P. E., "Stability of a Liquid Layer Adjacent to a High-Speed Gas Stream", *The Physics of Fluids*, vol. 8, no. 6, 1965.

[15]Nayfeh, A. H., Saric, W. S., 'Non-Linear Kelvin-Helmholtz Instability", *Journal of Fluid Mechanics*, vol. 46, part 2, pp. 209-231, 1971.

[16]Benjamin, T. B., "Shearing Flow over a Wavy Boundary", *Journal of Fluid Mechanics*, vol. 6, pp. 161-205, 1959.

[17]Gater, R. A. and L'Ecuyer, M. R. L., "A Fundamental Investigation of the Phenomena that Characterize Liquid Film Cooling", *International Journal of Heat and Mass Transfer* Vol. 13, pp 1925-1939, 1970.

[18]Nigmatulin, R., Nigmatulin, B., Khodzaev, Y. A. and Kroshilin, V., "Entrainment and Deposition Rates in a Dispersed-Film Flow", *International Journal of Multiphase Flow* Vol. 22, pp. 19-30, 1996.

[19]Ishii, M. and Grolmes, M. A., "Inception Criteria for Droplet Entrainment in Two Phase Concurrent Film Flow", *AICh Journal*, vol. 21, no. 2, pp. 308-318, 1975.

[20]Nigmatulin, B. I., Klebanonov, L. A., Kroshilin, A. E., "Heat transfer crisis for process steam-liquid dispersed annular flows under non-stationary conditions", *High Temp. Thermal Phys.* No. 18, 1242-1251, 1980.

[21]Marxman, G. A. "Combustion in the Turbulent Boundary Layer on a Vaporizing Surface", Tenth Symposium on Combustion, 1965, p 1337-1349.

[22]Karabeyoglu, M. A., Altman, D., Cantwell, B. J., Patent Pending, "High Regression Rate Hybrid Rocket Fuels"

[23]Dauber,T. E., Danner, R. T., "Physical and Thermodynamic Properties of Pure Chemicals, Data Compilation", Taylor and Francis, 1997.

[24]Altman, D. and Humble, R. "Hybrid Rocket Propulsion Systems" in Space Propulsion Analysis and Design, McGraw Hill, 1995, p382.

8) Tables and Figures

Propellant	Pentane C_5H_{12}	Acetone C_3H_6O	2,2,5 tmh C_9H_{20}	Oxygen O_2	HFI	Isopropanol C_3H_8O
Molecular Weight (g/mol)	72.15	58.08	128.26	32.0	69.11	60.10
Heat of Formation (kJ/mol)	-146.8	-217.2	-254.0	0.0	-231.7	-272.4
Surface Tension (mN/m)	14.3	19.2	11.3	13.2	15.6	16.4
Viscosity (mPa-sec)	0.46	0.51	0.42	0.33	2.5	5.0
Density-liquid phase (kg/m^3)	688.4	835.2	719.8	1226.9	785.0	808.9
Melting Temperature (K)	143.3	178.45	167.4	54.4	181	183.3
Boiling Temperature (K)	309.6	329.44	397.2	90.2	350	355.4
Heat of Fusion (kJ/kg)	116.7	98.0	48.3	13.7	96.3	89.4
Heat of Vaporization (kJ/kg)	357.8	513.0	261.8	190.58	540.2	663.4
Thermal Conductivity-liquid phase (W/mK)	0.14	0.17	0.12	0.17	0.137	0.14
Specific Heat-liquid phase (kJ/kg-K)	2.06	2.07	2.00	1.67	2.03	2.28
Specific Heat-solid phase (kJ/kg-K)	1.10	1.33	-	0.83	1.09	1.10
Entrainment Parameter[¶], Relative to Pentane	1	0.73	1.29	1.48	0.17	0.08
Burning Rate Characteristic	High	High	High	High	Low	Low

Table 1: Material properties of the propellants used in the calculations[23]. Liquid properties other than surface tension are evaluated at a mean temperature between the melting and vaporization temperatures. Surface tension is evaluated at the boiling temperature. See Ref. 10 for the estimation of properties for the mixture HFI.

[¶] Calculations are performed with the viscosity and surface tension exponents of 1 and 0.7, respectively.
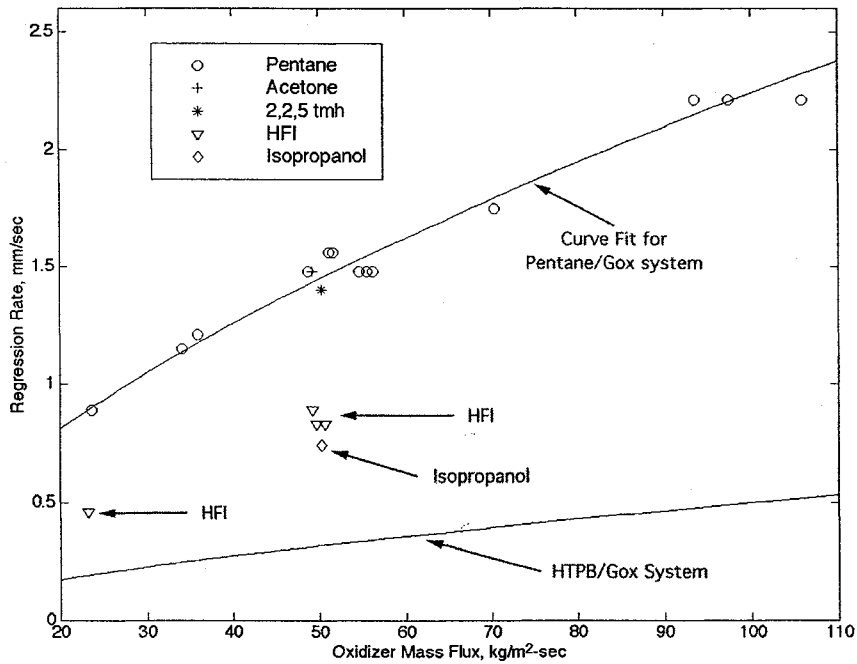
Figure 1: Space-time averaged regression rates are plotted versus the average oxidizer mass fluxes for various materials tested by AFRL. Curve fit expression for pentane data is $\dot{r} = 0.123\ G_o^{0.63}$ (i.e. $\dot{r}$ is in mm/sec and G_o is in kg/m²-sec). For comparison purposes the burning law of a classical propellant, HTPB, is included in the plot.
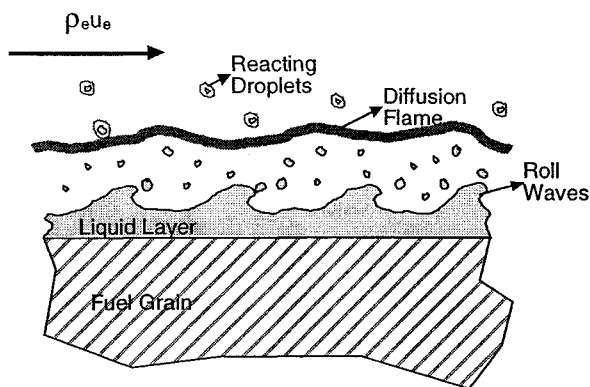
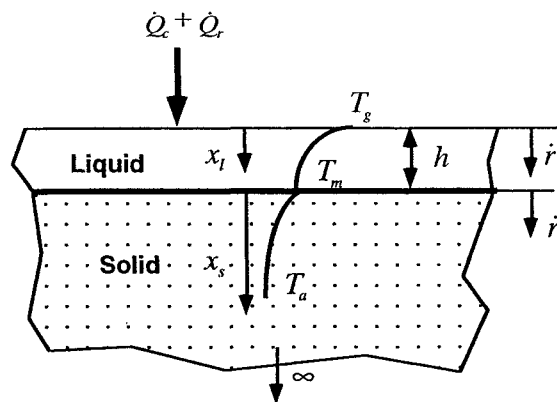

Figure 2: Schematic of the entrainment mechanism.

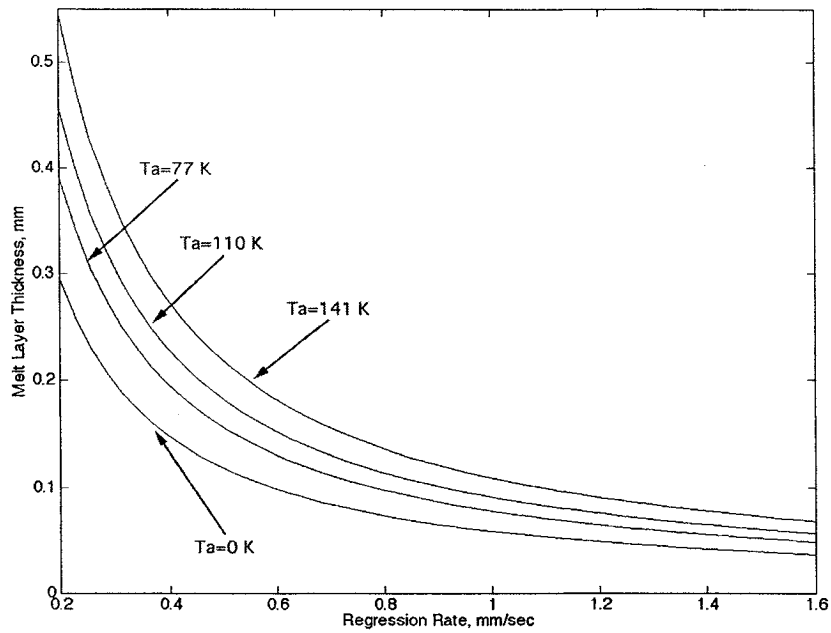**Figure 3:** Schematic of the thermal model used in the melt layer thickness estimation.

18

Figure 4: Effect of regression rate and initial slab temperature on the melt layer thickness for pentane.
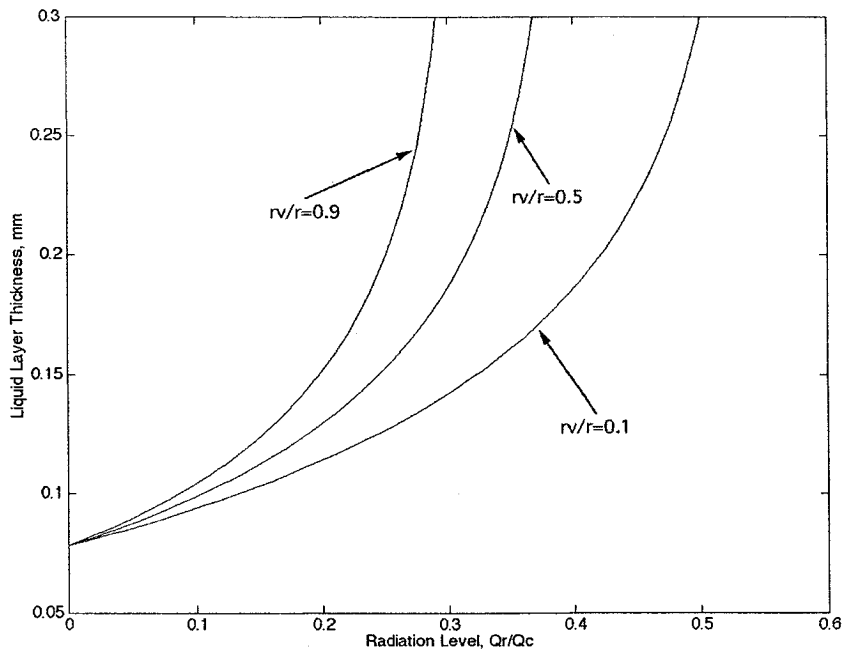
Figure 5: Effect of radiative heat transfer on the melt layer thickness of a pentane slab for various vaporization rates are plotted. The plots are for regression rate of 1 mm/sec and initial slab temperature of 77 K.
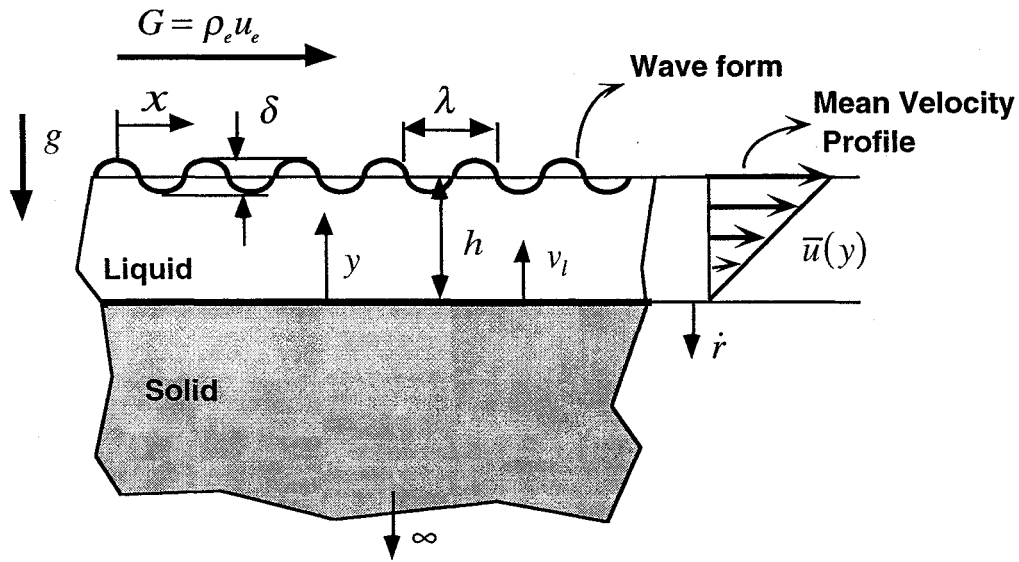
Figure 6: The schematic of the stability model.
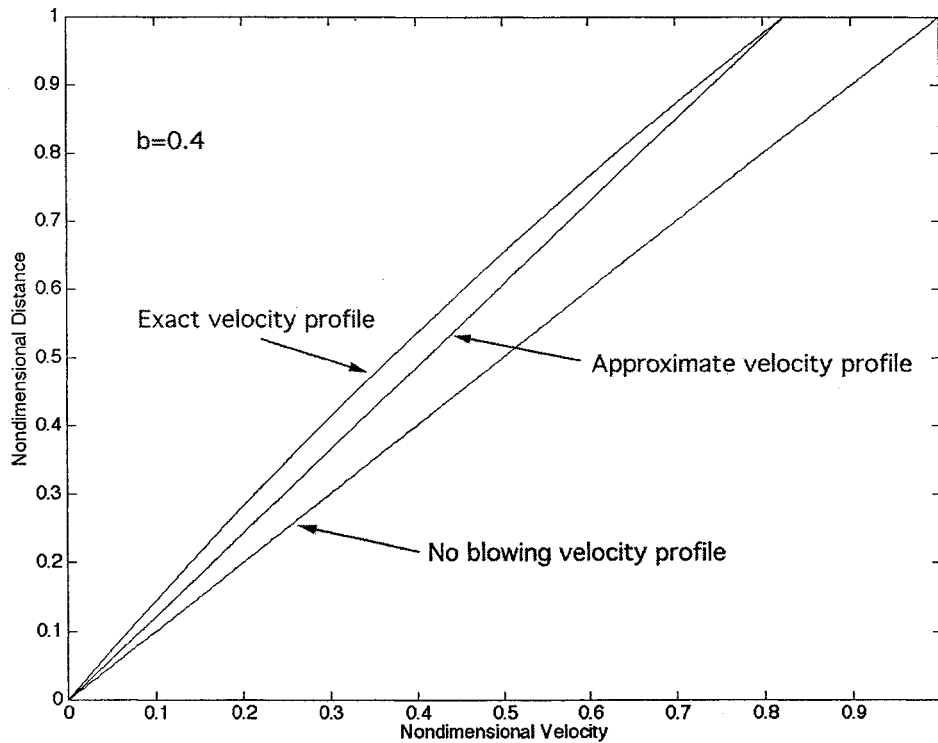
Figure 7: The exact velocity profile for the regression rate parameter of $b = 0.4$ the linear approximation given by Eqn.10 and also the velocity profile with no blowing are plotted.
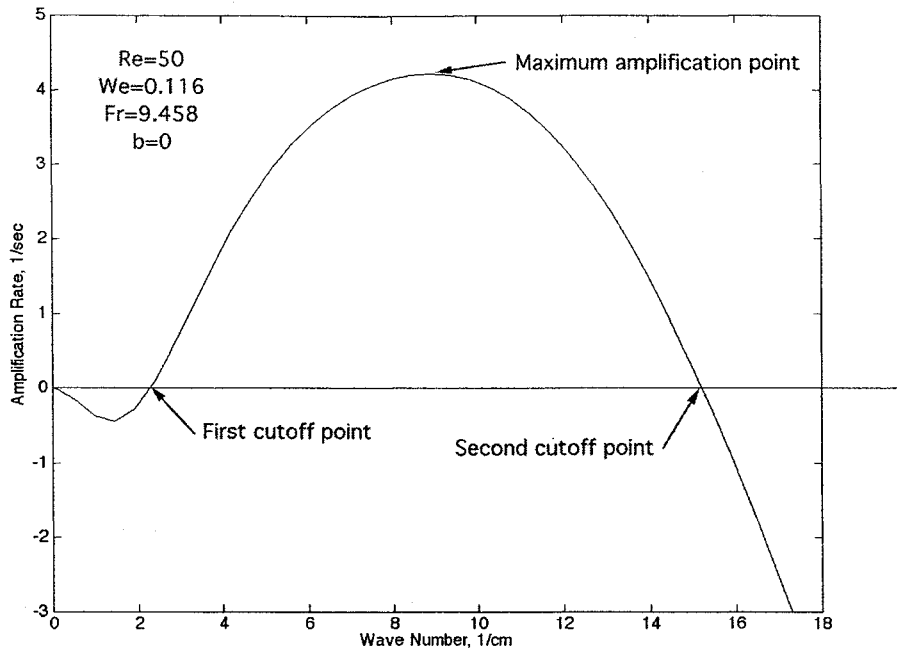
Figure 8: Amplification rate of a surface disturbance versus the wave number. This plot is for a water film with a thickness of 0.3 mm and film Reynolds number of 50. The Froude number is 9.458 and the regression rate parameter is zero.
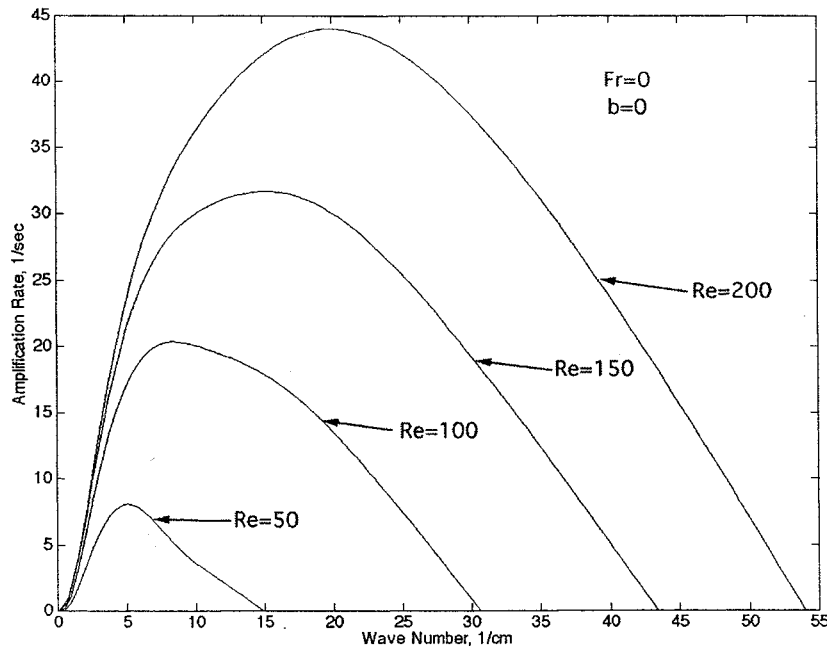
Figure 9: Amplification rate of a surface disturbance versus the wave number for various film Reynolds numbers. This plot is for a pentane film with a thickness of 0.3 mm. Reynolds number is altered by changing the gas mass flux in the port. The body force and the regression rate is taken to be zero for this calculation.

21
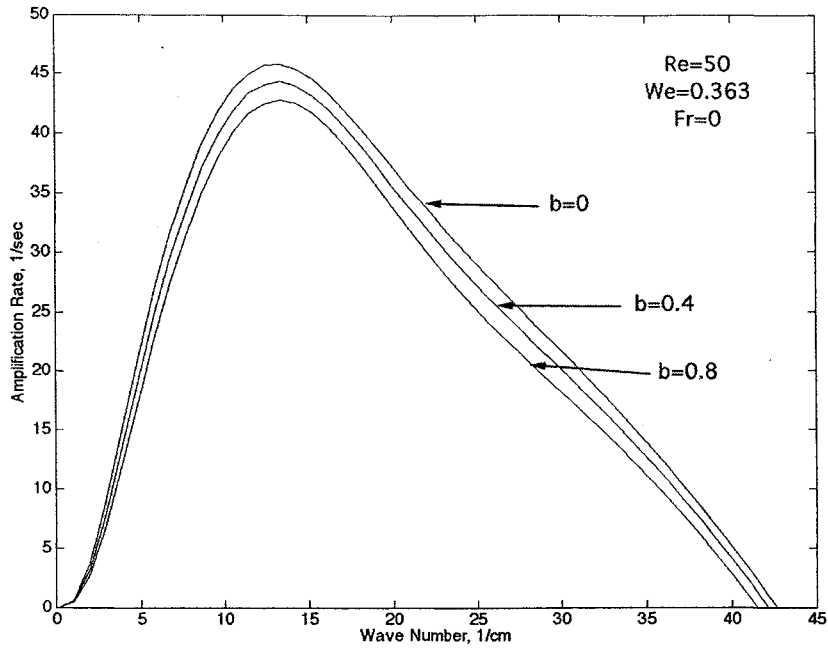
Figure 10: The effect of regression rate on the stability of the film is illustrated. This plot is for a pentane film with a thickness of 0.15 mm and a liquid Reynolds number of 50. The body force is taken to be zero.
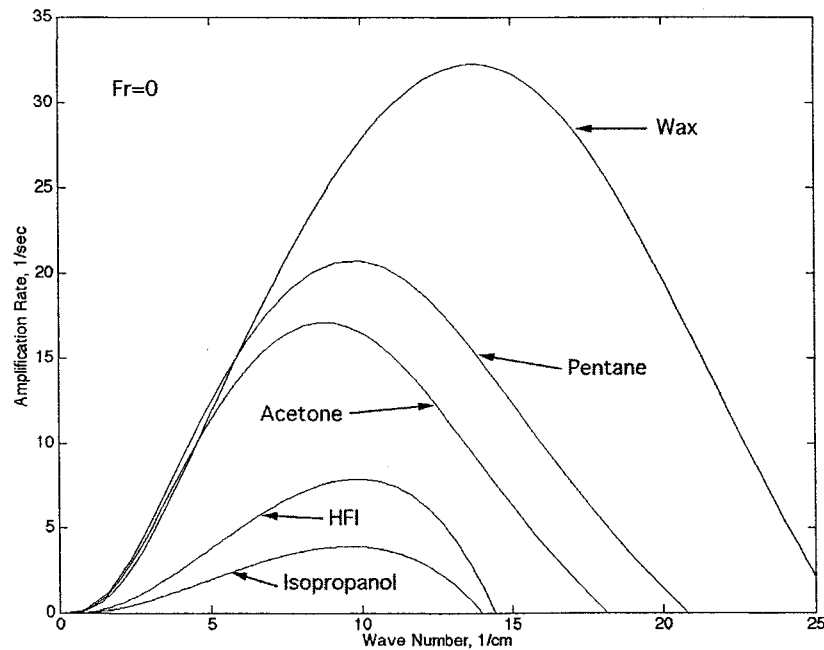

Figure 11: Amplification curves for various liquids for a port gas mass flux of 80 kg/m^2-sec and a regression rate of 1 mm/sec. A film thickness of 0.15 mm is used in these calculations. The body force is assumed to be zero.
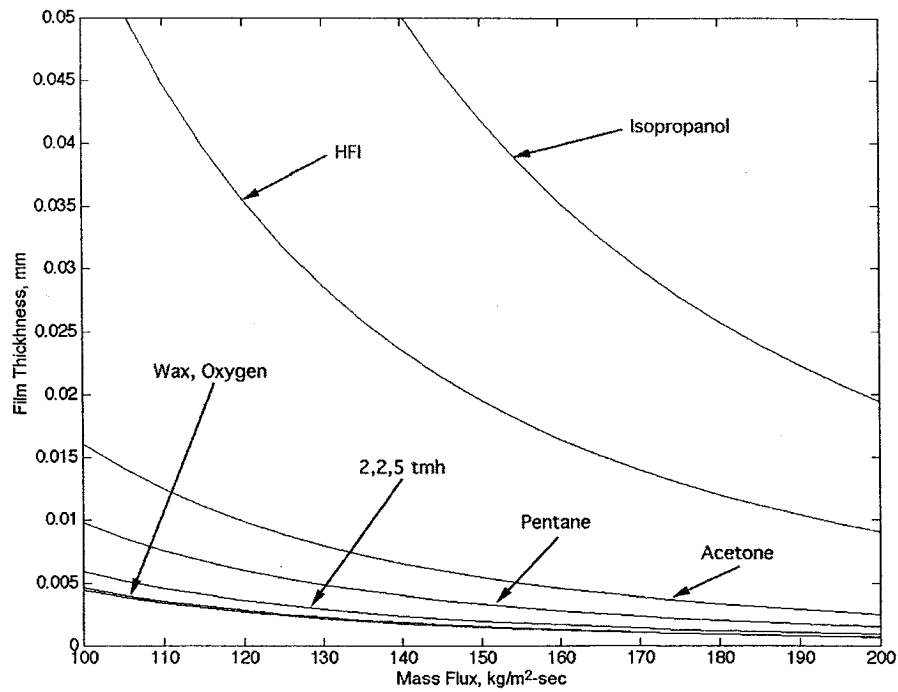
Figure 12: Entrainment onset boundaries in the thickness-mass flux plane for various propellants are plotted. Eq. 25 is used in the calculations.
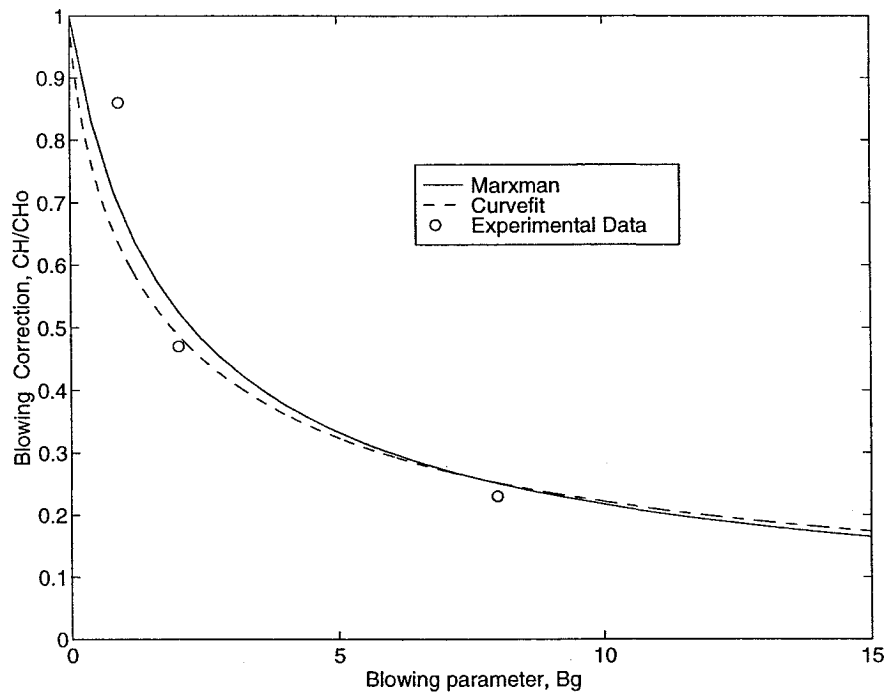

Figure 13: Blowing corrections according to Marxman's formula and our curve fit expression, Eq. 30, are plotted as a function of the blowing parameter. The experimental points are reported in Ref. 21.
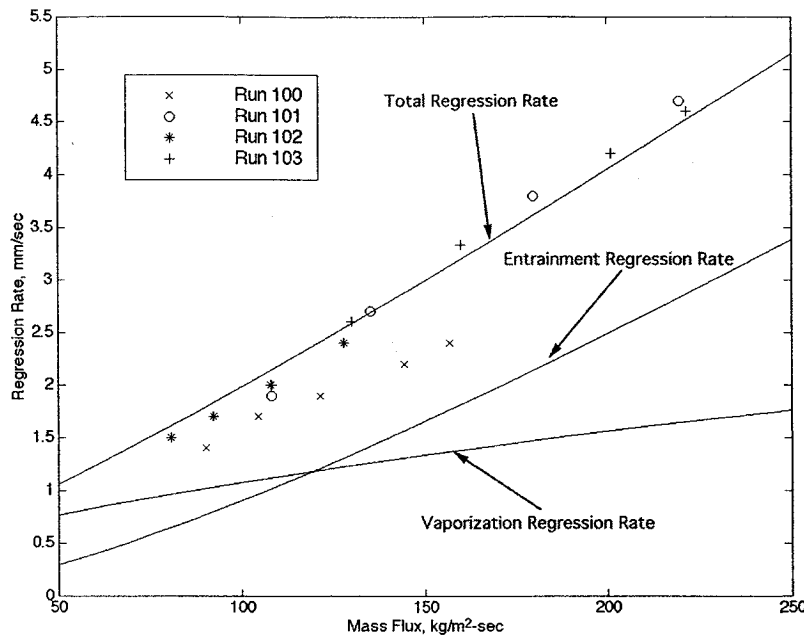
23

Figure 14: Estimates of instantaneous regression rates and corresponding mass fluxes evaluated at mid point of the port for 4 different pentane tests is plotted. Liquid layer theory predictions for the vaporization, entrainment and total regression rates are included in the plot.
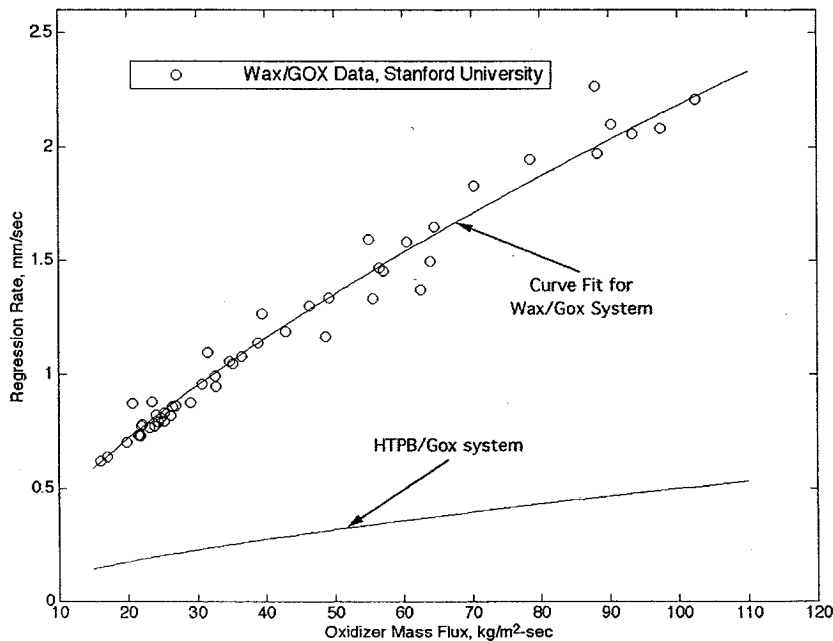

Figure 15: Space-time averaged regression rates are plotted versus the average oxidizer mass fluxes for the paraffin-based fuel (SP-1) tested at Stanford University. Curve fit expression for SP-1 data is $\dot{r} = 0.091 \ G_o^{0.69}$ (i.e. $\dot{r}$ is in mm/sec and G_o is in kg/m^2-sec). For comparison purposes the burning law of a classical propellant, HTPB, is included in the plot.